

A Novel α -Fe₂O₃/TiO₂ heterostructured nanocomposite with Enhanced Visible-light Photocatalytic Performance for Degradation of Organic Pollutant

Kavitha S

Government Arts college

Ranjith R

Periyar University

Jayamani N (✉ jayamaniphysics@gmail.com)

Government Arts college <https://orcid.org/0000-0002-5850-8849>

Research Article

Keywords: TiO₂/ α -Fe₂O₃, Visible-light, Photocatalysts, Methylene Blue, Dye degradation, Recycling stability, Hydroxyl radicals

Posted Date: February 16th, 2021

DOI: <https://doi.org/10.21203/rs.3.rs-198078/v1>

License:  This work is licensed under a Creative Commons Attribution 4.0 International License.

[Read Full License](#)

Abstract

A novel heterostructured catalyst of $\text{TiO}_2/\alpha\text{-Fe}_2\text{O}_3$ nanocomposite (NC) was successfully fabricated by the facile hydrothermal method and mutual ultrasonication. To characterize the as-fabricated photocatalysts (PCs) by PXRD, FT-IR, HRSEM, HRTEM, UV-Vis DRS absorption, and PL spectra analysis relatively. The optical absorbance of $\text{TiO}_2/\alpha\text{-Fe}_2\text{O}_3$ NC was measured in the wavelength range from $\sim 320\text{--}800\text{ nm}$ and the optical bandgap (E_g) was declined from 3.21 to 2.72 eV. The photocatalytic efficiency of $\text{TiO}_2/\alpha\text{-Fe}_2\text{O}_3$ composite catalyst was assayed in the degradation of aqueous methylene blue (MB) dye in the visible-light influence. The results showed that the heterostructured $\alpha\text{-Fe}_2\text{O}_3/\text{TiO}_2$ catalyst was much faster and higher removal efficiency of MB dye ($\sim 92.7\%$) than the other photocatalytic degradation of pristine TiO_2 (33 %) and $\alpha\text{-Fe}_2\text{O}_3$ (47.3 %) in 100 min. The enriched photocatalytic efficiency also accredited to enlarged energy harvesting ability, enhanced in the widened absorption in visible-light region, synergistic effects produced a great number of photo-produced electron-hole (e^-/h^+) separation, stronger oxidation ability by hydroxyl radicals ($\cdot\text{OH}$) via the interfaces of $\alpha\text{-Fe}_2\text{O}_3$ dispersed TiO_2 heterojunction. All these outcomes specify that the highly stable and recyclable $\text{TiO}_2/\alpha\text{-Fe}_2\text{O}_3$ photocatalyst has the possibility of the practical application for wastewater treatment.

Introduction

To meet the shortage in water supply worldwide and improving the environmental pollution, the elimination of several impurities from adequate water has major pervasive problem worldwide with widespread concerned. Nowadays the rapid industrialization of modern society exclusively in the developing countries, organic dyes are widely used in paper, leather, textile, pigment, cosmetic, food, and drug manufacturing [1–3]. Besides, the industrial and sanitary sewage comprises dyes cause water contamination as serious health problems and they are hazardous effects toward aquatic organisms, plants, humans, animals and aquatic ecosystem. Therefore, it is urgent to eliminate organic dyes from wastewaters. From former few decades, various techniques have been adopted to remove the dye-containing waters such as advanced oxidation processes (AOPs), physical adsorption, ozonation, photolysis and biological decomposition [3, 4]. Among them, semiconductors (SCs) heterogeneous photocatalytic AOPs decomposition has been expected to be effective strategies for used by many researchers since of its high degradation/mineralization efficiency to remove organic pollutants from wastewater due to the reactive $\cdot\text{OH}$, also low toxicity, low-cost, and ability to function under ambient settings [5].

Among various semiconductor photocatalysts (PCs), the well-known Titania (TiO_2) has attracted extensive courtesy owed to their preponderant potential features such as low-cost, non-toxicity, high photo-stability, fine electronic assets, great photochemical corrosive resistance, strong oxidizing power and photocatalytic movement [6–8]. This is based on the absorption of a photon of appropriate energy ($\sim 3.2\text{ eV}$) and the creation of charge carriers (photo-electrons (e^-) and photo-holes (h^+)) that could oxidize organic pollutants into CO_2 and H_2O . However, the practical application of TiO_2 catalyst is

hindered by the serious agglomeration of TiO_2 nanoparticles (NPs) and the quick recombination of the photo-produced (e^-/h^+) pairs [9, 10]. Moreover, the wide bandgap of TiO_2 limits its photocatalytic property in the ultraviolet (UV) region, which accounts for 3–5% of the total solar-light proportion spectrum. Since utilizing the visible-light is much more abundant (~ 43%) than UV light in the solar source, hence its efforts to synthesize efficient visible-light-responsive TiO_2 -based PCs are highly desired [11]. Several methods have been employed for enlightening the photocatalytic activity, the tremendous efforts are going to develop visible-light-driven (VLD) semiconductor PCs with heterojunction architecture for the TiO_2 PCs were coupled with various narrower bandgap SCs, such as CeO_2 , WO_3 , g-C₃N₄, MoS_2 , GO, Cu_2O , Fe_2O_3 and CdS [11–16].

Among diverse metal-oxides (MOs) semiconductor PCs, hematite ($\alpha\text{-Fe}_2\text{O}_3$) is kind of typical n-type SCs also facilitate the promising photocatalytic water splitting and water treatment applications. Because of its narrow bandgap (~ 2.0-2.2 eV), which exhibits excellent properties such as non-toxicity, environmentally friendly, natural abundance, superior chemical steadiness, high corrosion resistance, good conductivity, better visible-light fascination ability and solid oxidation power [17]. To resolve this inadequacy, it is an attractive route to organize the effective PCs by incorporating magnetic $\alpha\text{-Fe}_2\text{O}_3$, which not only prevents the agglomeration of other NPs during recovery but also deals the synergetic enrichment of catalytic activity to some extent by forming a hybrid structure [18]. Nevertheless, the photo-produced (e^-/h^+) pairs in the valence band (VB) and conduction band (CB) of $\alpha\text{-Fe}_2\text{O}_3$ are easier to be excited under visible-light exposure [19]. Besides, the coupling between $\alpha\text{-Fe}_2\text{O}_3$ and TiO_2 NPs forms most promising nanostructures (NSs) could support to the spatial electron (e^-) transfer, preventing the recombination of e^-/h^+ pairs and supplying more reaction active sites for widely improve the photocatalytic performance and recycling uses. Therefore, band bending might occur that the CB edge of $\alpha\text{-Fe}_2\text{O}_3$ is higher than that of TiO_2 when their Fermi levels are equalized [17]. As well, $\alpha\text{-Fe}_2\text{O}_3$ ions particularly adsorb on the negatively charged TiO_2 NPs by electrostatic dealings. Also, the modification of their band structures via unique properties of $\alpha\text{-Fe}_2\text{O}_3$ makes a suitable aspirant for coupling with TiO_2 would progress a new energy-level mismatch for visible-light photocatalysis. Therefore, $\alpha\text{-Fe}_2\text{O}_3$ has been extensively used as combined for VLD TiO_2 -based PCs by the hydrothermal assisted technique with the ultrasonic wave's supports. Since, hydrothermal assisted precipitation has applied most effective route among various techniques, to fabricate the effectual NPs and nanocomposites (NCs) samples due to its high purity, simple preparation, stoichiometry control and homogeneous distribution of coupling components [20]. Fortunately, Magnetic PCs might be proficiently separated and reprocessed by applying an external magnetic field.

In this existent document, a novel $\text{TiO}_2/\alpha\text{-Fe}_2\text{O}_3$ coupled heterogeneous photocatalyst were synthesized by facile hydrothermal assisted precipitation with then ultrasonic dispersion strategy. The as-fabricated NCs were characterized by various physicochemical analysis systems. Consequently, the effect of structural parameters, outstanding photocatalytic efficiency of MB dye decomposition under visible-light

treatment and excellent reusability of the used catalyst. Also, an interrelated major photocatalytic mechanism was proposed systematically.

2. Experimental

2.1. Materials and reagents

Sodium Hydroxide (NaOH) was obtained from Pure Chem Chemical Co., India. Titanium (IV) isopropoxide (TTIP, $\text{Ti}(\text{OC}_4\text{H}_9)_4$ 98.5 %) was attained since Alfa Aesar Chemical Co., India. ($(\text{FeCl}_3 \cdot 6\text{H}_2\text{O})$, 99 %), Polyvinylpyrrolidone (PVP, $(\text{C}_6\text{H}_9\text{NO})_n$ 98 %), 2-propanol ($\text{C}_{16}\text{H}_{21}\text{NO}_2$, 98 %) and Ethanol Absolute ($\text{C}_2\text{H}_6\text{O}$, 96 %), were attained from Merck Chemical Co., India. Entire chemicals were used here in analytical reagent (A.R) grade without auxiliary refinement, and reaction solutions were formed with high purity deionized (D.I.) water.

2.1 Material synthesis

The pristine TiO_2 NPs was fabricated by facile sol-gel process. Initially, the typical 5 mL of TTIP was added into 30 mL of 2-propanol solution. Then, the 0.1 g of PVP mixed with 20 mL of D.I. water was openly added to the solution through magnetically stirred for 60 °C at 4 h, next it was chilled and washed numerous times. Finally, the harvested TiO_2 NPs was dried overnight, and it's also crushed gently with mortar to acquire TiO_2 NPs [21]. The $\alpha\text{-Fe}_2\text{O}_3$ NPs were prepared via the precipitation route. In a typical experiment, 0.1 M $\text{FeCl}_3 \cdot 6\text{H}_2\text{O}$ and 0.1 g of PVP were dissolved in 100 mL of D.I. water and 50 mL of ethanol absolute solution composed under continuous vigorous stirring for 1 h at a temperature of 70 °C. Next, the ammonia aqueous solution was slow added dropwise into beyond colloidal suspensions to adjust the pH ~11 and subsequently aged at 60 °C. After naturally cooling at room temperature, the resultant dark red precipitates were obtained which were collected by centrifugation (3000 rpm), rinsed with D.I. water and ethanol to remove excess chlorine ions from the filtered material [22]. The obtained wet precipitous was then dried for 10 h at 80 °C and then calcined in air at 750 °C for 3 h to obtain $\alpha\text{-Fe}_2\text{O}_3$ NPs.

$\text{TiO}_2/\alpha\text{-Fe}_2\text{O}_3$ NC samples were also fabricated via the effective hydrothermal precipitation approach: As-fabricated TiO_2 and of $\alpha\text{-Fe}_2\text{O}_3$ NPs content were dispersed into ethanol and intensively sonicated for 30 min by probe ultrasonication. The resulting mixed suspension was after transferred into a 100 mL of Teflon-lined stainless steel autoclave and then finally treated at 150 °C for 5 h to attain $\text{TiO}_2/\alpha\text{-Fe}_2\text{O}_3$ heterogeneous composite in powder form [23].

2.2. Structural characterizations

Powder X-ray diffraction (XRD) analysis was passed out to define the crystal structure and phase of the as-fabricated PCs by Rigaku Miniflex II X-ray diffractometer, which was a Cu K α radiation ($\lambda = 1.54056 \text{ \AA}$). Fourier-transform infrared (FT -IR) spectra were noted on a Perkin Elmer RX-1 spectrometer via a KBr

pellet method in the ranges of 4000-400 cm⁻¹ for exploring the functional features. To identify surface morphologies and elemental configuration (weight %), High-resolution scanning electron microscope images, including Energy dispersive X-ray spectra (EDXS) were documented through HR-SEM; FEI Quanta FEG 200. The shape and deep microstructure were advance categorized by High-resolution Transmission electron microscopy (HRTEM) analysis consuming a JEOL/JEM 2100, operated at an accelerating voltage of 200 kV. UV-Vis diffuse reflectance spectroscopy (UV-Vis DRS) analysis was attained the optical absorption spectra on a UV2550; Shimadzu device. The room temperature photoluminescence (PL) spectral analysis was conceded out using a Perkin-Elmer-LS 100 by the excitation wavelength series on $\lambda_{ex} = \sim 330$ nm.

2.3. Photocatalytic activity

The photocatalytic acts of as-fabricated catalysts were assessed by VLD photodegradation with 50 mg of the as-fabricated PCs were dispersed into 20 ppm of MB aqueous dye solution injected into a 100 mL on the cylindrical quartz reflux system. To realize adsorption-desorption ability in the dark with actively stirred for 30 min. Then combined the decolourization performance scrutinized under the irradiation of visible-light and the 300 W -Xe lamp furnished by a reflection cutoff filter ($\lambda > 420$ nm) was resolute typically to prompt the photocatalytic response [24]. Every 20 minutes, to acquire nearly 2.0 mL of the liquid suspension was reserved out and centrifuged the pure solution was examined by UV-Vis spectra (Perkin Elmer-Lambda 35) at the utmost absorption band wavelength for MB (~664 nm) [25]. The photodecomposition removal efficiency % of MB dye was intended by the equation; Efficiency (%) = $(C_0 - C_t)/C_0 * 100$. Besides, the kinetic study of dye elimination enactment was deliberated agreeing to an equation of linear pseudo-first-order relation model, $-\ln(C_0/C_t) = kt$. Wherever C_t was the absorption found to MB dye in the preferred time intervals, k stands for the dye removal pseudo-first-order rate constant, C_0 has the initial absorbance of the MB dye at $t = 0$ min, and relative time t . For photocatalytic recycling trials, the investigational ailment was fixed as similar as aqueous MB photo-degradation format, and hence the catalysts have further washed, dried to succeeding reaction cycle [26]. The remaining concentration of aqueous MB dye was projected in each cycle for assessing the reusability of the as-fabricated PCs.

3. Results And Discussion

Figure 1 illustrates the XRD pattern of as-fabricated pristine TiO₂, α -Fe₂O₃ and TiO₂/ α -Fe₂O₃ NC samples. Crystalline planes consistent to the peaks for TiO₂ and α -Fe₂O₃ were well-indexed in this Fig. 1 (A). Numerous characteristic crystalline peaks are sensed for pristine TiO₂ sample at $2\theta = 25.2^\circ, 38.4^\circ, 48.2^\circ, 53.9^\circ, 55.2^\circ$ and 62.8° indexed to the (101), (112), (200), (105), (211) and (213) crystalline planes signifying the presence of prime TiO₂ tetragonal anatase crystallization phase (JCPDS file no. 21-1272) individually [18, 27]. Conversely, minor peaks are noticed at around 27.4° owed to the presence of a slight portion of TiO₂ rutile phase. Also, chief diffraction peaks at $24.3^\circ, 35.4^\circ, 40.7^\circ$ and 54.23° could be consigned to (012), (110), (113) and (116) crystal planes in the best contract (JCPDS file no. 01-1053)

with rhombohedral hematite α -Fe₂O₃ phase relatively. Accordingly, the XRD outcomes exposed that there effectively formation of α -Fe₂O₃ NPs on the TiO₂ provision. No further impurity peaks are noticed, specifying the high phase pureness of TiO₂/ α -Fe₂O₃ composite heterojunction has been fruitfully fabricated [28]. The average crystalline sizes of as-fabricated pristine TiO₂, α -Fe₂O₃ and TiO₂/ α -Fe₂O₃ catalysts were intended by Scherrer equation [1] and the detected values are 31, 19 and 23.5 nm separately. Hence, it's due to the substantial interface among the anatase and rhombohedral crystallites phases of TiO₂/ α -Fe₂O₃ composite and would stabilize the surfaces by precluding auxiliary evolution of crystallization.

The FT-IR spectra were employed to inspect the chemical bonding of the as-obtained NMs. Figure 2 displays the FT-IR spectra for as-fabricated pristine TiO₂, α -Fe₂O₃ and TiO₂/ α -Fe₂O₃ composites. The wide and high-intensity absorption peaks regions supposed under 800 cm⁻¹ (i.e.,) 462, 567 and 721 cm⁻¹ could be consigned to the grouping of Ti-O-Ti, Ti-O bond bridging stretching vibrations, and Fe-O asymmetric stretching, vibration kinds resulting from the chemical interface amid TiO₂ and α -Fe₂O₃ crystalline nanostructures designating that the co-presence of TiO₂ and α -Fe₂O₃ in the heterojunction [29, 30]. However, C = O and C-O are widening vibration absorption bands performed at 1753 and 1045 cm⁻¹ for almost atmospheric carbons in the FT-IR absorption spectra. The absorption peaks in the array of 2830–2980 cm⁻¹ agree to CH vibrations. The typical extensive absorptive peak regions at 1632 and 3451 cm⁻¹ are allotted to the OH bending and stretching vibrations appeared from free adsorbed water (H₂O) molecules respectively [31].

Fig. 3 (a) exhibits the HRSEM image of pristine TiO₂ NPs, while nanostructure observation exposes that the uniform circulation comprises irregularly shaped morphology. In Fig. 3 (b), it was found that the pristine α -Fe₂O₃ NPs have composed of the flake-like structures morphology and copious agglomerated certain dispersed NPs [32]. Also, it is observed that TiO₂/ α -Fe₂O₃ catalyst composite (Fig. 3 (c)) for the flake-like nanostructured α -Fe₂O₃ materials were self-possessed on TiO₂ assembly and fairly agglomerated with randomly distributed, which is supposed to be beneficial for augmenting the catalytic belongings [2]. Besides, EDXS spectrum was used to conclude the elemental weight ratio for the TiO₂/ α -Fe₂O₃ composite sample in Fig 3 (d). The outcomes exposed (insert Fig. 3 (d)) that the O, Ti and Fe elements were 42.11 %, 40.15 % and 17.74 % (weight %) relatively. The EDXS element mapping images (Fig. 4 (a-d)) of TiO₂/ α -Fe₂O₃ composite for auxiliary established that there spatial distribution and the pinpointed/isolated spots of the O, Fe and Ti elements [5,33]. Therefore, it is decided that TiO₂ NPs were effectively covered on the even superficial of cubic α -Fe₂O₃ NSs.

HRTEM images were demonstrated that α -Fe₂O₃ NPs were uniformly distribution decorated of NPs on the aggregation of TiO₂ surfaced spherical morphologies, as obtainable in Fig. 5 (a-f). What's more, the characteristic HR-TEM images have further disclosed that the composite maintains of flake-like structure with homogenous crumpled nanosheets [34]. The lattice fringes of as-achieved heterostructured TiO₂/ α -Fe₂O₃ composite typically exposed to the (101) facets of TiO₂ and (012) crystallographic planes of

α -Fe₂O₃ are discrete through measured the fringe spacing of 0.31 nm as presented in Fig. 5 (e, f). Hence the characteristic lattice lines for the selected area electron diffraction (SAED) pattern reveals the highly polycrystalline nature [6] of the NC in Fig. 5 (d). Also confirms the fruitful incorporation of both identical TiO₂ into α -Fe₂O₃ composite could be probable for the electrostatic interface among negatively charged TiO₂ and positively charged α -Fe₂O₃ NPs which is augmenting the charge carriers separation also notable for enlightened photocatalytic enrichment of TiO₂/ α -Fe₂O₃ catalyst [35]. These consequences were which suggest in good promise with that of the XRD outcomes.

To investigate the UV-Vis DRS absorbance spectra of as-fabricated samples were shown in Fig. 6 (A). As revealed in Fig. 6, the UV-Vis absorption edges of pristine TiO₂ NPs are about \sim 325 nm in the spectra, whereas endorsed to the electronic transition of O_{2p} to Ti_{3d} [36]. For pristine α -Fe₂O₃ NPs exhibit, apparent visible-light absorption is detected in the curve (λ_{ab} upto \sim 590 nm). In contrast, the TiO₂/ α -Fe₂O₃ composite catalyst presented not only stronger light absorption threshold in the UV region of less than \sim 390 nm, then the suitable and robust absorption edges found in the visible-light province of \sim 400–700 nm could be witnessed in Fig. 6 (A). These fallouts which proposed that they TiO₂ were red-shifted into the visible-light after adding the α -Fe₂O₃, hence it has been stated the charge transfer by the direct transition from O_{2p} to Fe³⁺ (3d) could change the visible absorbance to the elongated wavelength from the indirect transition among Fe³⁺ (3d) electrons (e⁻) [27]. Hence, it has not only encourage the separation and migration of photo-produced charges but also contribute to the CB in the upper situation. Thus, the UV-Vis spectra effects proved the incorporation of Fe³⁺ in TiO₂. Remarkably, this would be extended the visible-light photocatalytic movement of the heterostructured TiO₂/ α -Fe₂O₃ composite photocatalyst, also utilized by realizing the solar light [37].

Figure 6 (B) illustrates the Tauc plots of $(ahv)^2$ versus photon energy (hv) for the optical bandgap energies of as-attained catalysts, which were intended founded on the optical absorption edge attained from UV-Vis DRS spectra using Kubelka-Munk Eqn; $ahv = A (hv - E_g)^{n/2}$. Wherever, A, E_g, a, h, v, are the relatively constant, bandgap energy, absorption coefficient, Planck's constant, incident light frequency, and where, n = $\frac{1}{2}$, and 2 for direct and indirect bandgap consistently [32]. The outcomes show that the intercepts of band-gap energies of pristine TiO₂, α -Fe₂O₃ and TiO₂/ α -Fe₂O₃ PCs are estimated roughly 3.21, 2.11, and 2.72 eV, individually. In the existing form, Fe³⁺ was mixed with the TiO₂ lattice, ensued in the decreasing the bandgap of TiO₂ NPs, greatly upgraded to enabled the visible-light fascination assets of the heterostructured TiO₂/ α -Fe₂O₃ PCs [38]. As advised for owed to an exclusive electronic arrangement, implying that the Fe³⁺ has the ability to the form novel narrowing energy levels occurs in the bandgap of TiO₂ NPs and declines the bandgap with active photo-excitation between VB and CB. This might be correlated to particle size, surface morphology and the novel accumulation of α -Fe₂O₃, as well the Fermi level of TiO₂/ α -Fe₂O₃ heterostructured NC hints to energy bandgap declined [39]. Conferring to the UV-Vis DRS outcomes, the as-fabricated TiO₂/ α -Fe₂O₃ PCs with a narrow bandgap are projected to

expose the outstanding photocatalytic action for decomposing organic impurities in the visible-light expanse, which agreed to the VLD photo-degrading manner [40].

PL emission spectra could be carried out to explore the efficiency of photo-produced (e^-/h^+) pairs, transfer, separation, trapping, immigration and to understand the rate of charge-carrier recombination in the specified semiconductor PCs, as one of the essential factors disturbing the photocatalytic exploit. Figure 7 (A) confirms the PL spectra of as-obtained heterostructured PCs and the emission intensity peaks of the as-fabricated pristine TiO_2 , α - Fe_2O_3 and TiO_2/α - Fe_2O_3 catalyst were at 461, 447 and 459 nm, congruently. The PL emission peak of TiO_2 was upper than that of TiO_2/α - Fe_2O_3 NC which designated that occurrence of α - Fe_2O_3 reduced the (e^-/h^+) recombination rate [41]. In contrast, novel configurations of the heterostructure amongst α - Fe_2O_3 and TiO_2 NMs which declines the PL emission intensity of the near band edge emission (NBE) and might owed to the intrinsic/extrinsic luminescence defects related NBE. The Fe^{3+}/Fe_2O_3 ions could be integrated into the TiO_2 lattice either by substituting Fe^{3+} ions fashioning especially ionized oxygen vacancies (V_o) or as interstitial of Fe^{3+} . So the lesser PL emission intensity of the TiO_2/α - Fe_2O_3 PCs has a significant for the extent of charge separation are specifies the effectively restrained recombination rate primary to admirable light-harvesting capability hence, the photocatalytic efficacy was heightened [28].

Photocatalytic activity analysis

The photocatalytic efficiency of as-fabricated TiO_2/α - Fe_2O_3 PCs was widely evaluated by the decomposition of MB dye and the absorption peak declined steadily under visible-light exposure (Fig. 7 (B)) at diverse time intermission from 0 min to 100 min [37]. Also, the MB aqueous solution alone without photocatalyst (blank) was directed to check the self-photodegradation of MB dye have exceptionally low and with under dark situation in the existence of PCs hence it has negligible [25]. The photo-degradation efficacy of C/C_0 curves for MB over as-fabricated TiO_2 and α - Fe_2O_3 catalysts were only 33 % and 47.7 %, individually. Moreover, the TiO_2/α - Fe_2O_3 heterostructured composite catalyst resulting in the superior photocatalytic activity (92.7 %) could be achieved amongst all the as-fabricated PCs after 100 mins of visible-light exposure. Figure 8 (A) demonstrates the consistent concentration changes of the MB aqueous dye solution and the response rate (k) as a function of visible-light exposure time [35]. The photo-degradation proficiencies of MB aqueous dye by as-obtained PCs are originated to the succeeding order: TiO_2/α - $Fe_2O_3 > \alpha$ - $Fe_2O_3 > TiO_2$.

In order to quantitatively discover the kinetics of MB dye photodegradation under visible-light exposure for the as-fabricated PCs were investigated as shown in Fig. 8 (B), and this suggests that pseudo-first-order kinetics reaction rates. The specious reaction rate constants (k) for as-fabricated TiO_2 , α - Fe_2O_3 and TiO_2/α - Fe_2O_3 PCs were determined as 0.0071 min^{-1} , 0.0109 min^{-1} , and 0.0252 min^{-1} relatively. It was found that the maximum photocatalytic performance for the decomposition of MB aqueous dye, which was about 3.54 and 2.31 times greater that of as-fabricated TiO_2 and α - Fe_2O_3 catalyst under the identical

conditions respectively [42]. Besides to photocatalytic efficacy, the stability of the specified photocatalyst is also essential for practical use for the handling of organic impurities in wastewater [30]. To inspect the reusability and stability of $\text{TiO}_2/\alpha\text{-Fe}_2\text{O}_3$, the PCs after photocatalysis progression were composed and reused for five successive times under the identical settings. As publicized in Fig. 9 (A), the $\text{TiO}_2/\alpha\text{-Fe}_2\text{O}_3$ PCs revealed noble reusability throughout five photo-decomposition reuses [37]. After five recycles of photo-reduction of MB dye, the $\text{TiO}_2/\alpha\text{-Fe}_2\text{O}_3$ PCs did not display any significant loss of activity Fig. 8 (A), hence it's understood the stability of catalyst after four consecutive catalytic reprocess. Since there was a substantial drop in the fifth recycle (80.6 %), which was ascribed to the loss of $\alpha\text{-Fe}_2\text{O}_3$ catalyst during the recycling reaction. The crystalline structure and their functional groups were characterized by XRD and FT-IR individually. Hence the $\text{TiO}_2/\alpha\text{-Fe}_2\text{O}_3$ PCs have almost no obvious structural changes were found in before and after the photocatalytic recycles investigates (Fig. 10 (A) and (B)) which outcomes signifying a good stable adequate for recycling [43]. Therefore, $\text{TiO}_2/\alpha\text{-Fe}_2\text{O}_3$ heterostructured PCs are projected to be promising in environmental remediation since not only tremendous photocatalytic stability, also enabled energy conversion in the visible-light region [44, 45]. In contrast, with the earlier reported literature of various NCs for photodegradation of organic impurities, $\text{TiO}_2/\alpha\text{-Fe}_2\text{O}_3$ composite PCs have displayed superb removal efficacy for MB dye, as tabularized in Table 1.

To validate the radicals of NCs in the photocatalytic decomposition process, the trapping investigates of reactive species are executed. Figure 9 (B) displays the three diverse quenching manners, for instance, 0.5 mM of isopropanol (IPA), disodium ethylene diamine-tetra acetate (EDTA-2Na), and benzoquinone (BQ) were used to sense the scavengers of hydroxyl radicals (% $\cdot\text{OH}^-$), holes (% h^+) and superoxide anion radicals (% $\cdot\text{O}_2^-$) absolutely [41]. As could be realized in Fig. 8 (B) the decomposition rate of PCs slightly decreases corresponding to the adding of BQ and EDTA-2Na, signifying that which % h^+ and % $\cdot\text{O}_2^-$ are the slight responsive species on this concerned structures. Nevertheless, the accumulation of IPA caused apparent deactivation of the photocatalyst, decreasing the photocatalytic movement for the decomposition rated from 92.7 % to 16 % as exposed in the quenching investigation outcomes. This noticeably validates that active $\cdot\text{OH}^-$ radicals are the foremost reactive species liable for VLD photocatalytic decolourization scheme over these $\text{TiO}_2/\alpha\text{-Fe}_2\text{O}_3$ heterostructured PCs [46].

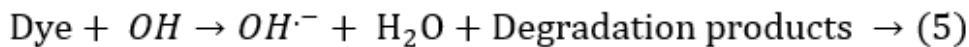
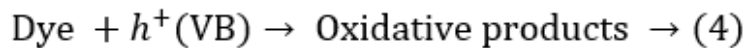
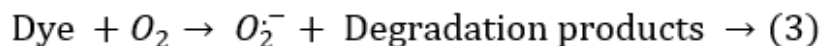
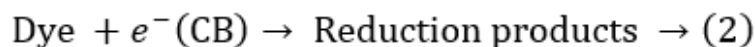
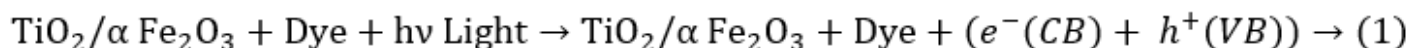
Table 1
Comparison of VLD photocatalytic degradation of MB dye (%) over of previous literature reported catalytic NMs

S. No.	Photocatalysts	Dye	Irradiation time (min.)	Degradation efficiency (%)	Ref.
1.	Ga-Ag/ZnO	MB	300	~ 39	[44]
2.	P25 TiO ₂	MB	300	~ 48	[47]
3.	CNTs/TiO ₂ /Ag	MB	240	~ 48	[48]
4.	ZnO/SnO ₂	MB	240	~ 90	[49]
5.	TiO ₂ /CeO ₅	MB	150	~ 95	[30]
6.	CdS/TiO ₂	MB	180	~ 63	[25]
7.	Fe ₂ O ₃ /Cu ₂ O	MB	80	~ 40	[50]
8.	TiO ₂ /α-Fe ₂ O ₃ PCs	MB	100	~ 92.7	This work

On the base of the upstairs debate, it is noticeable that the generation and (e^- - h^+) separation process mechanism could be proficiently indorsed by the interface between TiO₂ and α-Fe₂O₃ catalyst under visible-light exposure [28]. The VB and CB edge potential position could be gathered via according to the Mulliken electronegativity theory for following Eqn; $E_{VB} = \chi - E_e + 0.5 E_g$ and $E_{CB} = E_{VB} - E_g$. Wherein, χ signifies the absolute Mulliken electronegativity of given SCs (χ TiO₂ = 5.81 eV, and χ α-Fe₂O₃ = 5.88 eV), separately [51]. Moreover, the E_g , E_e , E_{VB} and E_{CB} were energy bandgap of specified SCs by UV-DRS spectra (E_g of TiO₂ = 3.21 eV; E_g of α-Fe₂O₃ = 2.11 eV), the energy of free electrons on the hydrogen scale (ca. 4.5 eV), VB edge potential and CB edge potential individually [52]. Agreeing to the above equations, the energy level diagram is based upon the E_{VB} and E_{CB} values were estimated to be of TiO₂ (E_{VB} = 2.915, E_{CB} = -0.295) and its favorable than α-Fe₂O₃ (E_{VB} = 2.48, E_{CB} = 0.28) discretely.

Based on the upstairs analysis and conversation, the photo-produced charge separation and transfer of the TiO₂/α-Fe₂O₃ heterostructured catalyst for the improved plausible photocatalytic action in visible-light preservation could be anticipated as exposed above trial outcomes in Fig. 11. Under the visible-light illumination ($\lambda > 420$ nm), both the SCs catalysts of TiO₂ and α-Fe₂O₃ catalyst are photo-excited primarily by photons while to produce more electron-hole (e^- - h^+) pairs, which are then separated and stimulated to diverse ways under the reaction energy [32]. In detail, the photo-electrons (e^-) of TiO₂ will transfer to the CB of α-Fe₂O₃, meanwhile, the photo-holes (h^+) of α-Fe₂O₃ will transport to the VB of TiO₂ (Ti 3d) under the exploit of a built-in electric field. Though, under the energetic reaction in the photo-electrons (e^-) of α-Fe₂O₃ and the photo-holes (h^+) of TiO₂ would exchange to both other and then concluding the

consequence of (e^- - h^+) recombination. In photocatalytic system, the photo-electrons (e^-) prompt to the reduction of Fe^{3+} ions to Fe^{2+} ions [50]. When α - Fe_2O_3 NPs were united with TiO_2 NPs, the Fermi level of TiO_2 and α - Fe_2O_3 necessity align in symmetry owed to the occurrence of the TiO_2/α - Fe_2O_3 heterojunction [27]. The authority of TiO_2/α - Fe_2O_3 NSs also profits from the pairing by narrow bandgap semiconductor α - Fe_2O_3 . Thus the (e^- / h^+) recombination progression is greatly suppressed and efficient (e^- / h^+) separation is realized on the NC surface [47]. In this case, the presence of TiO_2/α - Fe_2O_3 fitted heterostructures, the conversion of the photo-electrons (e^-) and the photo-holes (h^+) would primary go through the hybrid layer simply owed the firm migration rate position which also stimulates the outstanding charge separation movement. Concurrently, the samples of TiO_2 and α - Fe_2O_3 PCs will efforts to the photo-oxidation and reduction situates also the virtual interesting water oxidation for the photodegradation reaction could be attained, exclusively [1]. Also, the photo-electrons (e^-) in the VB of TiO_2 was auxiliary respond with molecular oxygen O_2 dissolved in the solution to form the superoxide anion ($O_2\cdot^-$) and hydrogen peroxide (H_2O_2). Consecutively, the photodegradation of MB dye is reached by capture the photo-electrons (e^-) and the photo-holes (h^+) could also oxidize either the organic molecule directly and/or the OH ions H_2O fragments are adsorbed on the catalytic surface to the sturdy oxidizing to reactive ' OH^- ' radicals by the end products on the photocatalyst surface [42]. Our consequences exposed that the construction of TiO_2/α - Fe_2O_3 PCs hinder the recombination of photo-excited electron-hole (e^- - h^+) pairs and encourage the generation of more ' OH^- ' radicals resulted in the development of photodegradation competence of TiO_2/α - Fe_2O_3 PCs [25]. While the amassed photo-holes (h^+) in the VB of Fe_2O_3 respond with OH^- species or H_2O^\cdot prevailing on the surface of the PCs, fabricating responsive hydroxyl radicals (' OH^- ') which are auxiliary intricate in the photodegradation of MB dye, as presented in Fig. 11. To conclude, the organic-acids were photo-oxidized to form into the harmless ingredients of CO_2 and H_2O [53, 54]. This reaction could be responsible for specified by equations (1)-(5);



4. Conclusion

In summary, TiO_2/α - Fe_2O_3 composite catalysts were efficiently fabricated by hydrothermal assisted precipitation manner and enhanced VLD photocatalytic actions were also surveyed. The powder XRD diffraction pattern peaks of TiO_2 and α - Fe_2O_3 NPs were well accorded with the tetragonal (anatase) and rhombohedral phases are obtained. The narrow bandgap of α - Fe_2O_3 was engaged to outspread the

optical response of TiO_2 to the visible-light region. Though $\text{TiO}_2/\alpha\text{-Fe}_2\text{O}_3$ sample has revealed the premier photocatalytic action of the organic MB aqueous dye among other as-fabricated TiO_2 and $\alpha\text{-Fe}_2\text{O}_3$ PCs in the visible-light region. The photocatalytic materials also exhibit adequate superior cyclic stability and the dye decomposition efficiency could be 80.6 % after five successive cycle runs. It is accredited to the well-suited interface fashioned heterojunction structures between TiO_2 and $\alpha\text{-Fe}_2\text{O}_3$, which promotes the efficient photo-produced (e^- - h^+) charge transfer/separation, restraining the recombination rate, with prolonged optical absorption into the visible region and favourable ' OH^- ' radicals invention ability. To conclude, a promising photocatalytic mechanism is projected for this novel PCs. Here consider that the expansion of the great photocatalytic actions of $\text{TiO}_2/\alpha\text{-Fe}_2\text{O}_3$ heterostructures will deliver an auspicious platform for the highly stable and reusable performance of photocatalytic practical applications.

Declarations

The authors have declares no conflict of interest.

References

1. G.K. Upadhyay, J.K. Rajput, T.K. Pathak, V. Kumar, L.P. Purohit, Vacuum **160**, 154 (2019)
2. Y. Koo, G. Littlejohn, B. Collins, Y. Yun, V.N. Shanov, M. Schulz, D. Pai, J. Sankar, Composites Part B: Engineering **57**, 105 (2014)
3. S. He, P. Hou, E. Petropoulos, Y. Feng, Y. Yu, L. Xue, L. Yang, Front. Chem. **6**, 1 (2018)
4. M. Wang, Y. Hu, J. Han, R. Guo, H. Xiong, Y. Yin, Journal of Materials Chemistry A **3**, 20727 (2015)
5. L. Kong, J. Yan, P. Li, S.F. Liu, ACS Sustainable Chemistry and Engineering **6**, 10436 (2018)
6. G.R. Surikanti, A.K. Bandarapu, M.V. Sunkara, ChemistrySelect **4**, 2249 (2019)
7. P. Pooseekheaw, W. Thongpan, A. Panthawan, E. Kantarak, W. Sroila, P. Singjai, Molecules **25**, 3327 (2020)
8. W.K. Jo, T. Adinaveen, J.J. Vijaya, N.C. Sagaya, Selvam, RSC Advances **6**, 10487 (2016)
9. A. Leelavathi, B. Mukherjee, C. Nethravathi, S. Kundu, M. Dhivya, N. Ravishankar, G. Madras, RSC Advances **3**, 20970 (2013)
10. J. Sun, X. Li, Q. Zhao, J. Ke, D. Zhang, J. Phys. Chem. C **118**, 10113 (2014)
11. M.S.S. Danish, A. Bhattacharya, D. Stepanova, A. Mikhaylov, M.L. Grilli, M. Khosravy, T. Senju, Metals **10**, 1604 (2020)
12. W. K. Jo and N. Clament Sagaya Selvam, Journal of Hazardous Materials 299, 462 (2015)
13. S. Martha, P. Chandra Sahoo, K.M. Parida, RSC Advances **5**, 61535 (2015)
14. C. Karthikeyan, P. Arunachalam, K. Ramachandran, A.M. Al-Mayouf, S. Karuppuchamy, J. Alloy. Compd. **828**, 154281 (2020)
15. S. Gautam, H. Agrawal, M. Thakur, A. Akbari, H. Sharda, R. Kaur, M. Amini, Journal of Environmental Chemical Engineering **8**, 103726 (2020)

16. A. Gołębiewska, M.P. Kobyłański, A. Zaleska-Medynska, in *Metal Oxide-Based Photocatalysis: Fundamentals and Prospects for Application* (Elsevier, 2018), pp. 3–50
17. M.M. Mohamed, W.A. Bayoumy, M.E. Goher, M.H. Abdo, and T. Y. Mansour El-Ashkar, *Applied Surface Science* **412**, 668 (2017)
18. W.K. Jo, N.C.S. Selvam, *Dalton Trans.* **44**, 16024 (2015)
19. L. Xu, J. Wang, *Environ. Sci. Technol.* **46**, 10145 (2012)
20. S. Balu, S. Velmurugan, S. Palanisamy, S.W. Chen, V. Velusamy, T.C.K. Yang, and E. S. I. El-Shafey, *J. Taiwan Inst. Chem. Eng.* **99**, 258 (2019)
21. L. Baia, E. Orbán, S. Fodor, B. Hampel, E.Z. Kedves, K. Saszet, I. Székely, É Karácsonyi, B. Réti, P. Berki, A. Vulpoi, K. Magyari, A. Csavdári, C. Bolla, V. Coșoveanu, K. Hernádi, M. Baia, A. Dombi, V. Danciu, G. Kovács, Z. Pap, *Mater. Sci. Semicond. Process.* **42**, 66 (2016)
22. A.M. Abdel-Wahab, A.S. Al-Shirbini, O. Mohamed, O. Nasr, *J. Photochem. Photobiol., A* **347**, 186 (2017)
23. S. Ma, S. Zhan, Y. Jia, Q. Zhou, *ACS Applied Materials and Interfaces* **7**, 10576 (2015)
24. D. He, Y. Yang, J. Tang, K. Zhou, W. Chen, Y. Chen, Z. Dong, *Environ. Sci. Pollut. Res.* **26**, 12359 (2019)
25. H. Wei, L. Wang, Z. Li, S. Ni, Q. Zhao, *Nano-Micro Letters* **3**, 6 (2011)
26. K. Kaviyarasan, V. Vinoth, T. Sivasankar, A.M. Asiri, J.J. Wu, S. Anandan, *Ultrason. Sonochem.* **51**, 223 (2019)
27. X. Lu, X. Li, F. Chen, Z. Chen, J. Qian, Q. Zhang, *J. Alloy. Compd.* **815**, 152326 (2020)
28. J. Tian, P. Hao, N. Wei, H. Cui, H. Liu, *ACS Catalysis* **5**, 4530 (2015)
29. B. Singaram, K. Varadharajan, J. Jeyaram, R. Rajendran, V. Jayavel, *J. Photochem. Photobiol., A* **349**, 91 (2017)
30. J.C. Cano-Franco, M. Álvarez-Láinez, *Mater. Sci. Semicond. Process.* **90**, 190 (2019)
31. M. Fakhrul Ridhwan Samsudin, S. Sufian, R. Bashiri, N. Muti Mohamed, L. Tau, Siang, R. Mahirah, Ramli, *Materials Today: Proceedings* **5**, 21710 (2018)
32. W.A. Aboutaleb, R.A. El-Salamony, *Mater. Chem. Phys.* **236**, 121724 (2019)
33. L. Zhu, H. Li, Z. Liu, P. Xia, Y. Xie, D. Xiong, *J. Phys. Chem. C* **122**, 9531 (2018)
34. S. Chandrasekaran, W.M. Choi, J.S. Chung, S.H. Hur, E.J. Kim, *Mater. Lett.* **136**, 118 (2014)
35. V. Ramasamy Raja, A. Karthika, S. Lok Kirubahar, A. Suganthi, M. Rajarajan, *Solid State Ionics* **332**, 55 (2019)
36. D. Lu, B. Zhao, P. Fang, S. Zhai, D. Li, Z. Chen, W. Wu, W. Chai, Y. Wu, N. Qi, *Appl. Surf. Sci.* **359**, 435 (2015)
37. N.S. Arul, D. Mangalaraj, R. Ramachandran, A.N. Grace, J.I. Han, *Journal of Materials Chemistry A* **3**, 15248 (2015)
38. B. Sharma, P.K. Boruah, A. Yadav, M.R. Das, *Journal of Environmental Chemical Engineering* **6**, 134 (2018)

39. J. Qin, C. Yang, M. Cao, X. Zhang, R. Saravanan, S. Limpanart, M. Ma, R. Liu, Mater. Lett. **189**, 156 (2017)
40. G.K. Upadhyay, J.K. Rajput, T.K. Pathak, V. Kumar, L.P. Purohit, Vacuum **160**, 154 (2019)
41. L. Rožić, S. Petrović, D. Lončarević, B. Grbić, N. Radić, S. Stojadinović, V. Jović, J. Lamovec, Ceram. Int. **45**, 2361 (2019)
42. L. Zhu, H. Li, Z. Liu, P. Xia, Y. Xie, D. Xiong, J. Phys. Chem. C **122**, 9531 (2018)
43. A.B. Ali Baig, V. Rathinam, J. Palaninathan, Applied Water Science **10**, 54 (2020)
44. M.N. Cardoza-Contreras, A. Vásquez-Gallegos, A. Vidal-Limon, J.M. Romo-Herrera, S. Águila, O.E. Contreras, Catalysts **9**, 1 (2019)
45. Y. Lei, J. Huo, H. Liao, RSC Advances **7**, 40621 (2017)
46. A.B. Ali Baig, V. Rathinam, V. Ramya, Materials Technology **1** (2020)
47. M. Gurulakshmi, M. Selvaraj, A. Selvamani, P. Vijayan, N.R. Sasi, Rekha, K. Shanthi, Appl. Catal. A **449**, 31 (2012)
48. Y. Koo, G. Littlejohn, B. Collins, Y. Yun, V.N. Shanov, M. Schulz, D. Pai, J. Sankar, Composites Part B: Engineering **57**, 105 (2014)
49. M.M. Rashad, A.A. Ismail, I. Osama, I.A. Ibrahim, A.-H.T. Kandil, Arabian Journal of Chemistry **7**, 71 (2014)
50. S.K. Lakhera, R. Venkataramana, A. Watts, M. Anpo, B. Neppolian, Res. Chem. Intermed. **43**, 5091 (2017)
51. R. Saravanan, V.K. Gupta, E. Mosquera, F. Gracia, J. Mol. Liq. **198**, 409 (2014)
52. D. Zhang, S. Cui, J. Yang, J. Alloy. Compd. **708**, 1141 (2017)
53. R. Li, Y. Jia, N. Bu, J. Wu, Q. Zhen, J. Alloy. Compd. **643**, 88 (2015)
54. Z. Zhang, Y. Ma, X. Bu, Q. Wu, Z. Hang, Z. Dong, X. Wu, Sci. Rep. **8**, 10532 (2018)

Figures

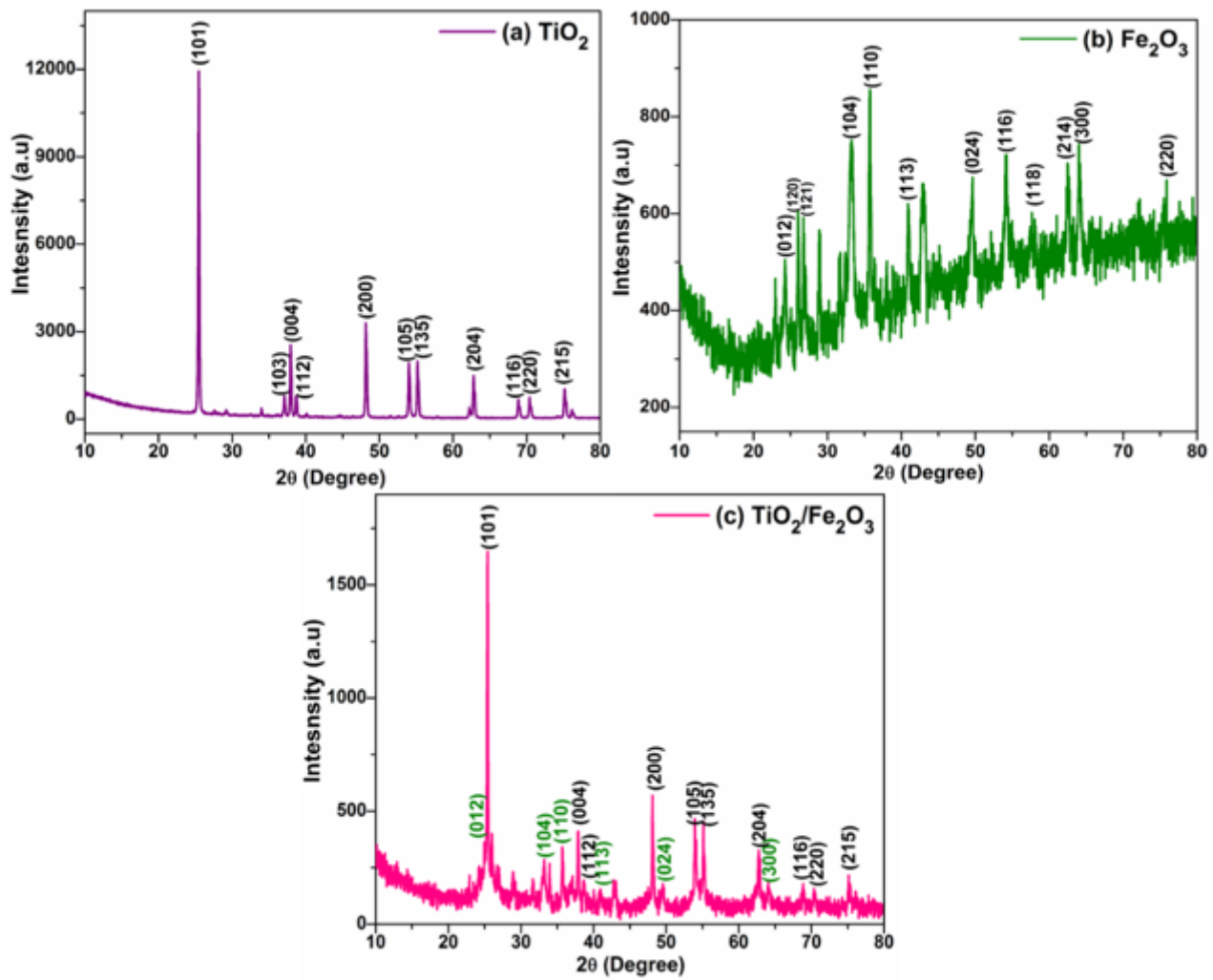


Figure 1

Powder XRD pattern of as-obtained samples

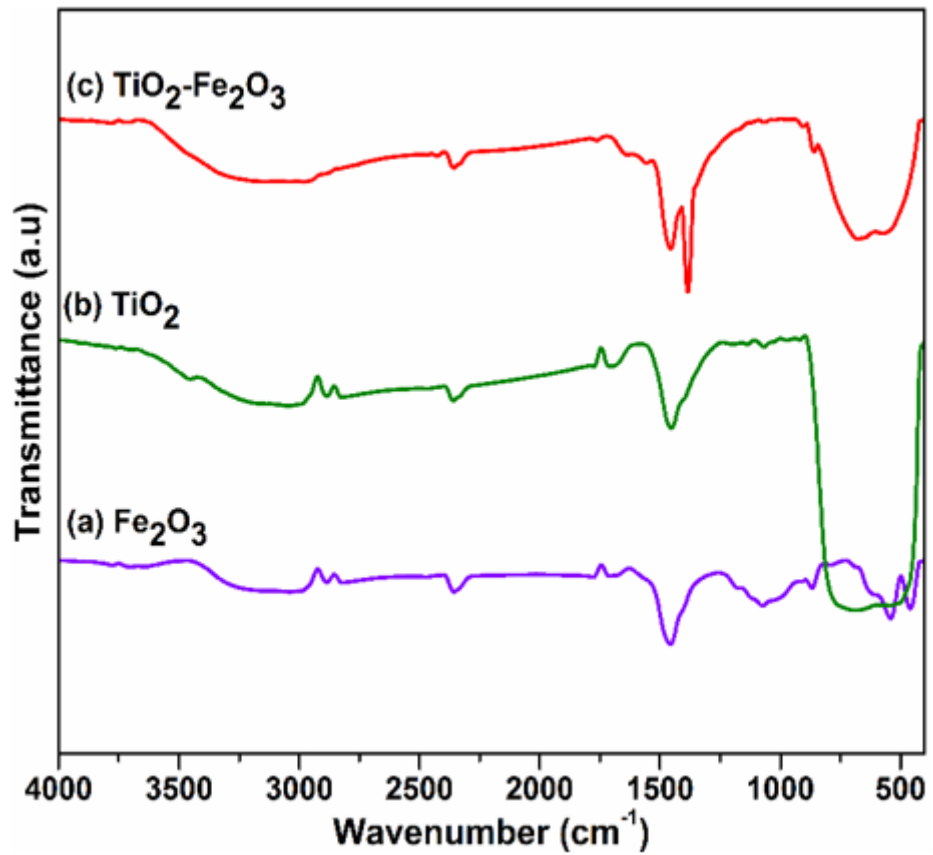


Figure 2

FT-IR spectra of as-obtained samples

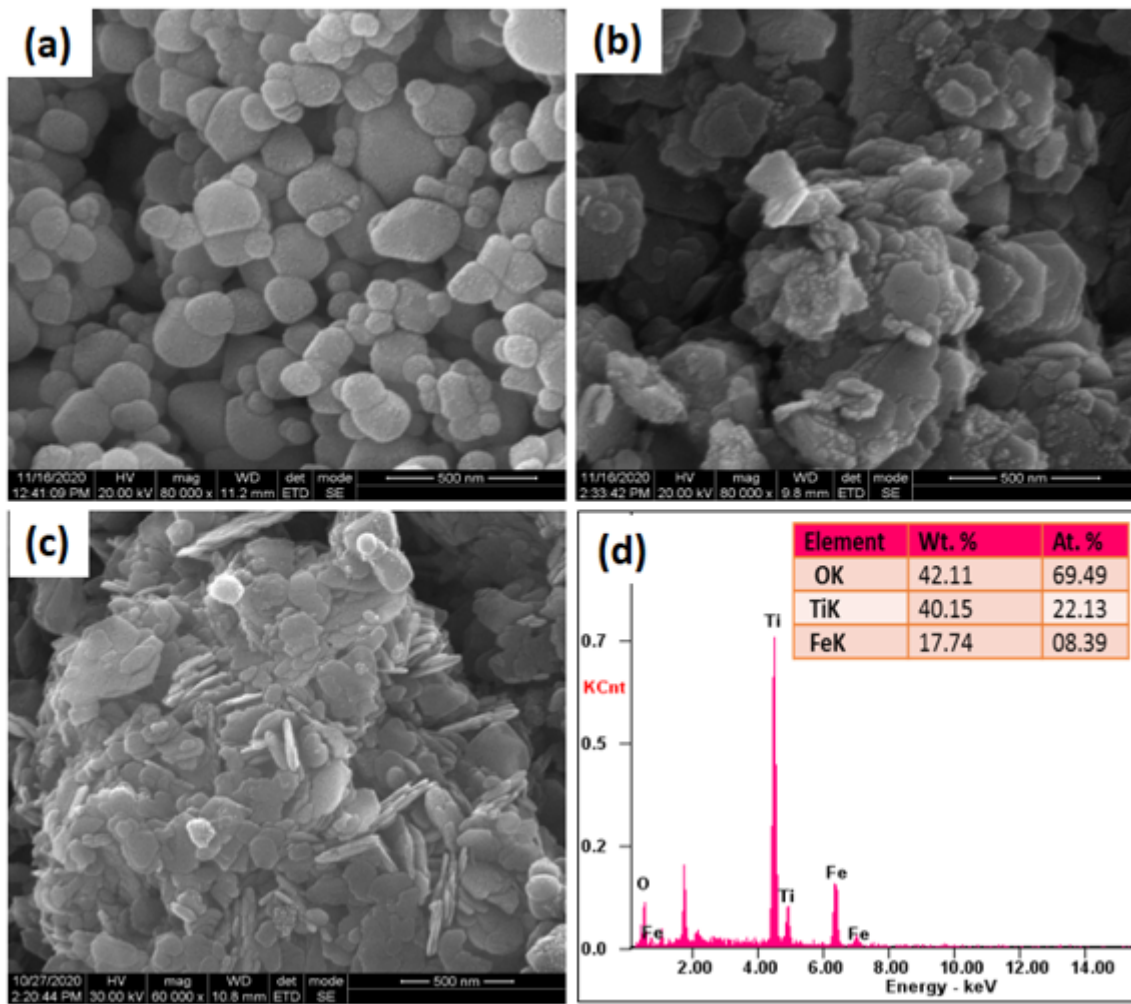


Figure 3

HRSEM images of as-fabricated (a) pristine TiO₂ (b) α-Fe₂O₃ (c) TiO₂/α-Fe₂O₃ composite and (d) consistent EDXS spectrum of TiO₂/α-Fe₂O₃ composite

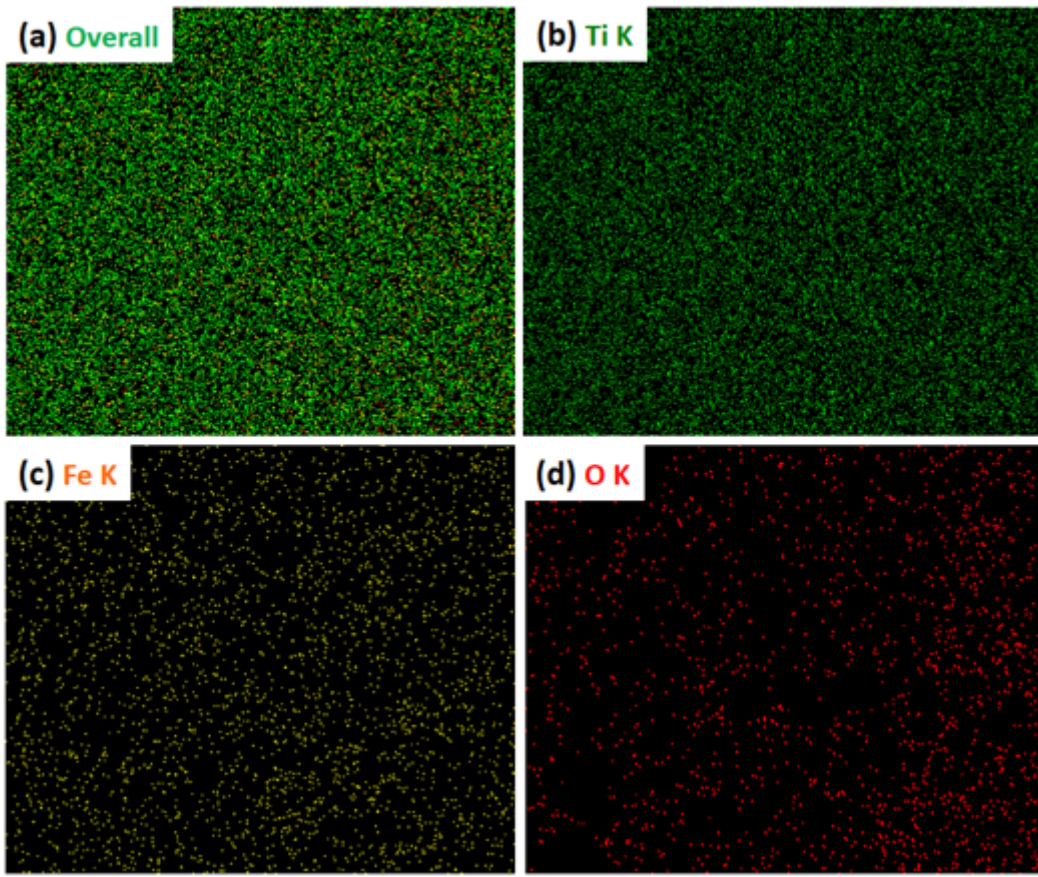


Figure 4

EDXS elemental mapping of $\text{TiO}_2/\alpha\text{-Fe}_2\text{O}_3$ NC; Pictures of (b) Ti, (c) Fe and (d) O elements

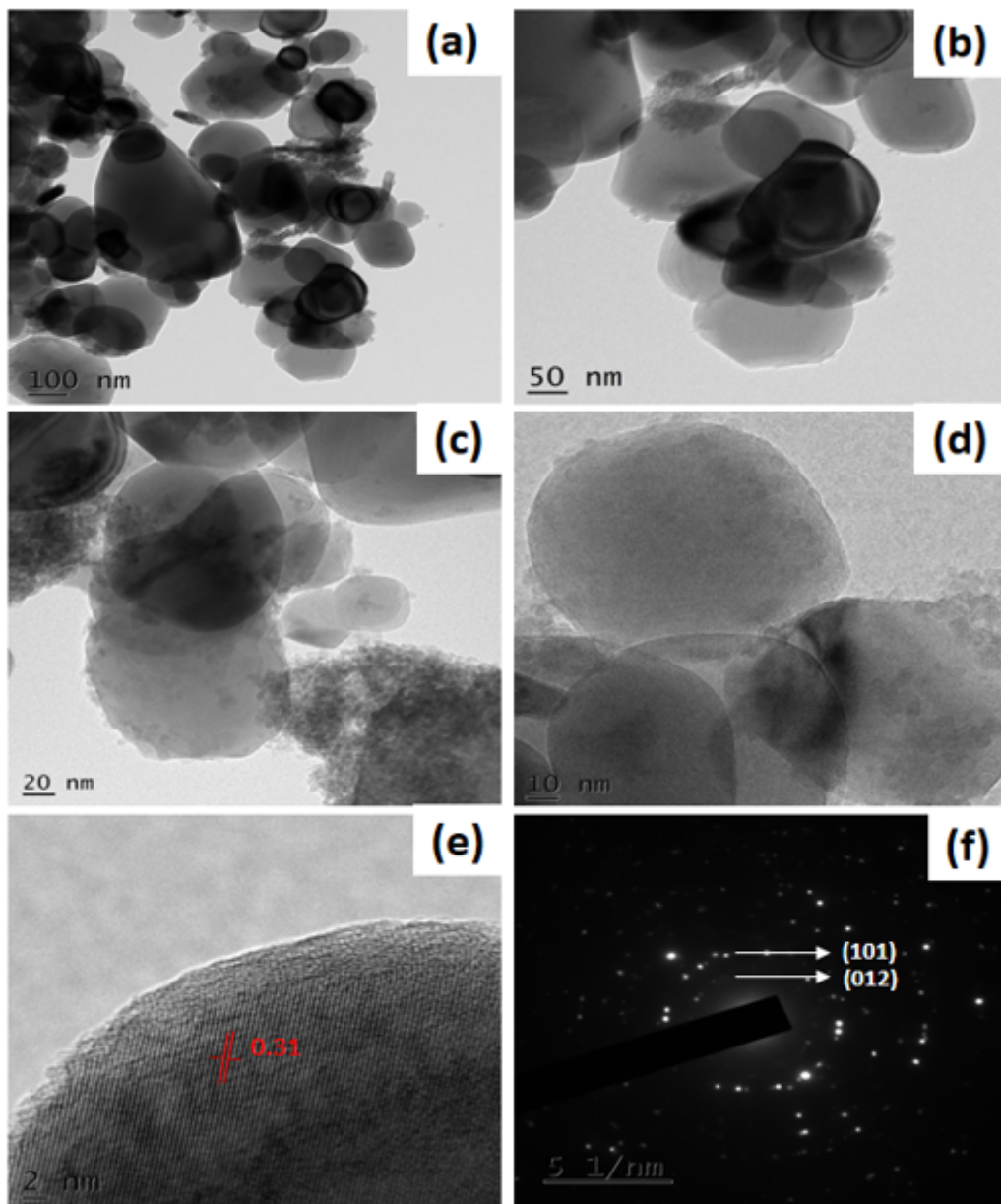


Figure 5

Typical HRTEM images of as-fabricated $\text{TiO}_2/\alpha\text{-Fe}_2\text{O}_3$ heterostructured composite

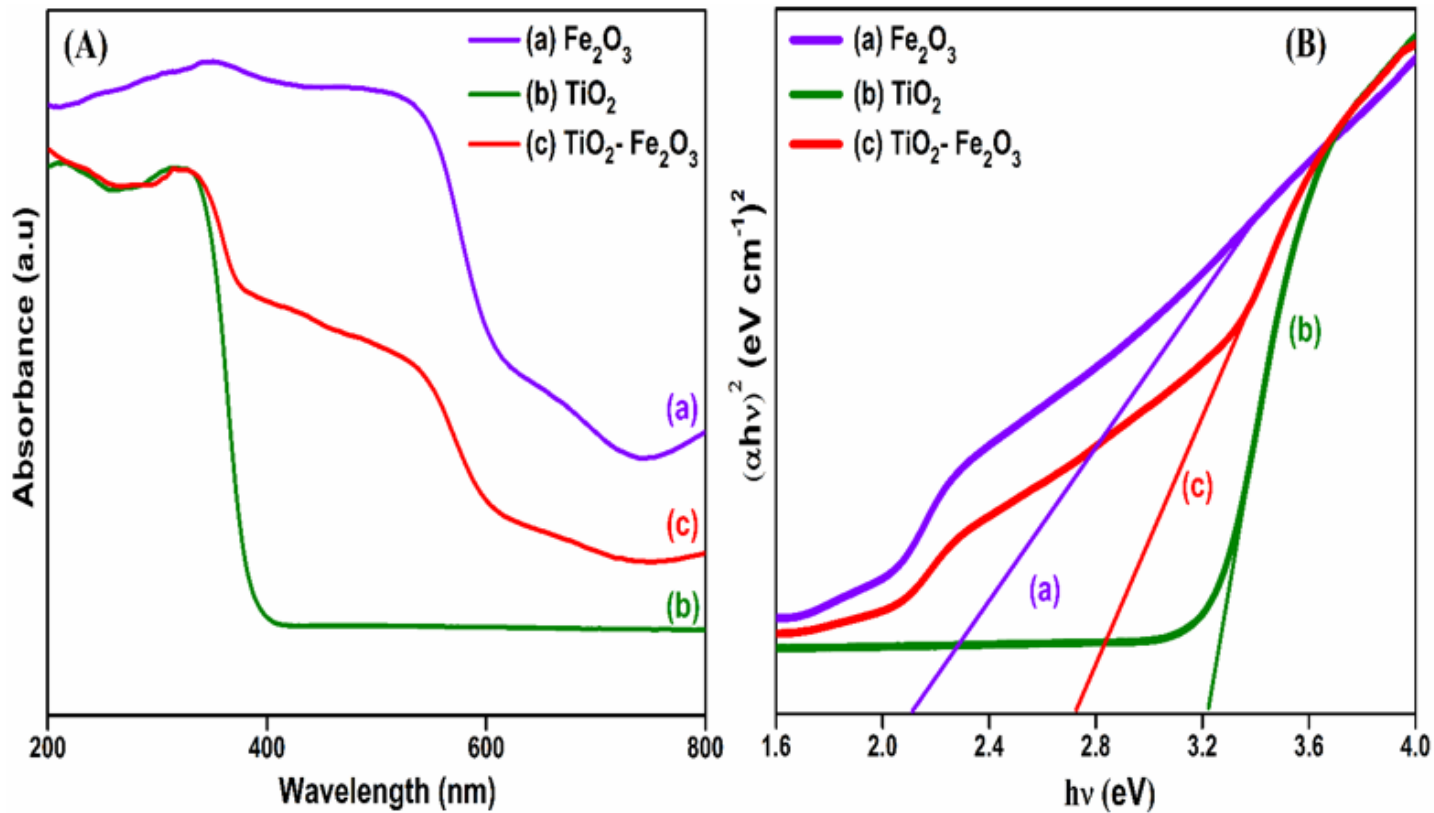


Figure 6

(A) UV-Vis DRS optical absorption spectra (B) relative Tauc plot of as-fabricated (a) pristine TiO_2 (b) $\alpha\text{-Fe}_2\text{O}_3$ (c) $\text{TiO}_2/\alpha\text{-Fe}_2\text{O}_3$ NMs

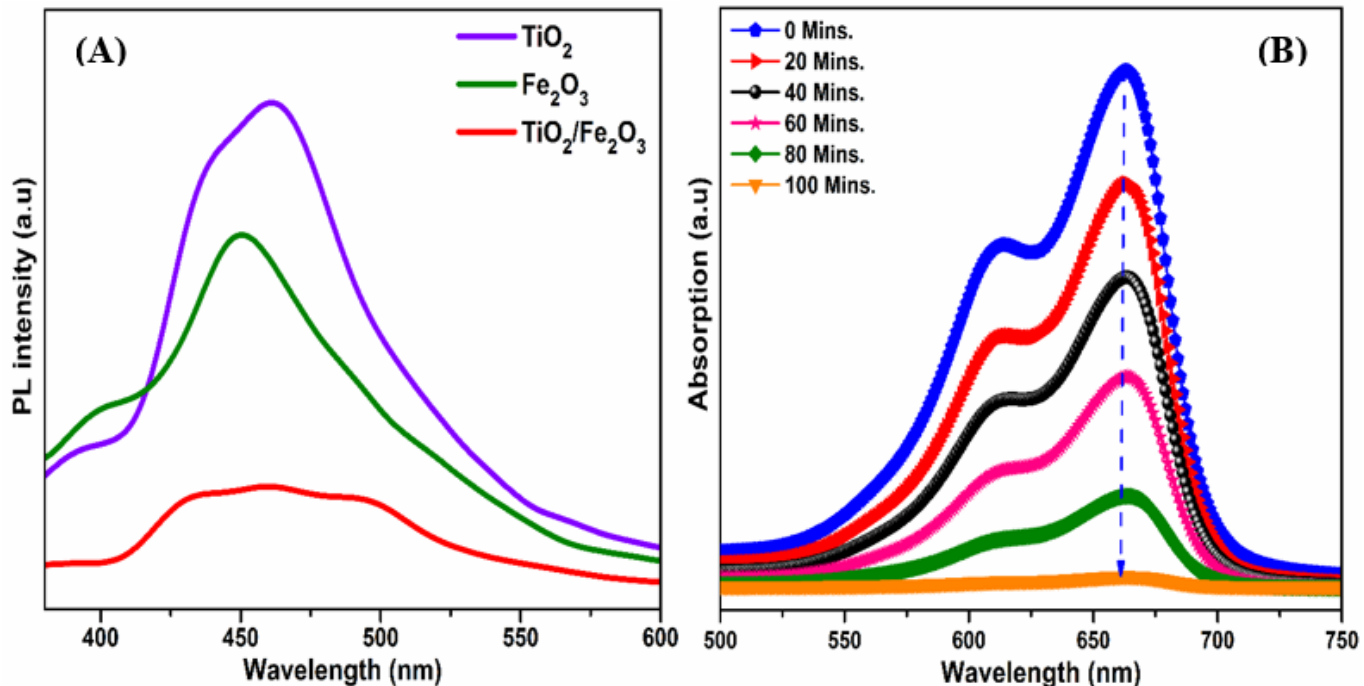


Figure 7

(A) Room-temperature PL spectra, $\lambda_{\text{ex}} \sim 330$ nm; and Photocatalytic degradation of MB over the TiO₂/α-Fe₂O₃ composite catalyst under visible-light exposure

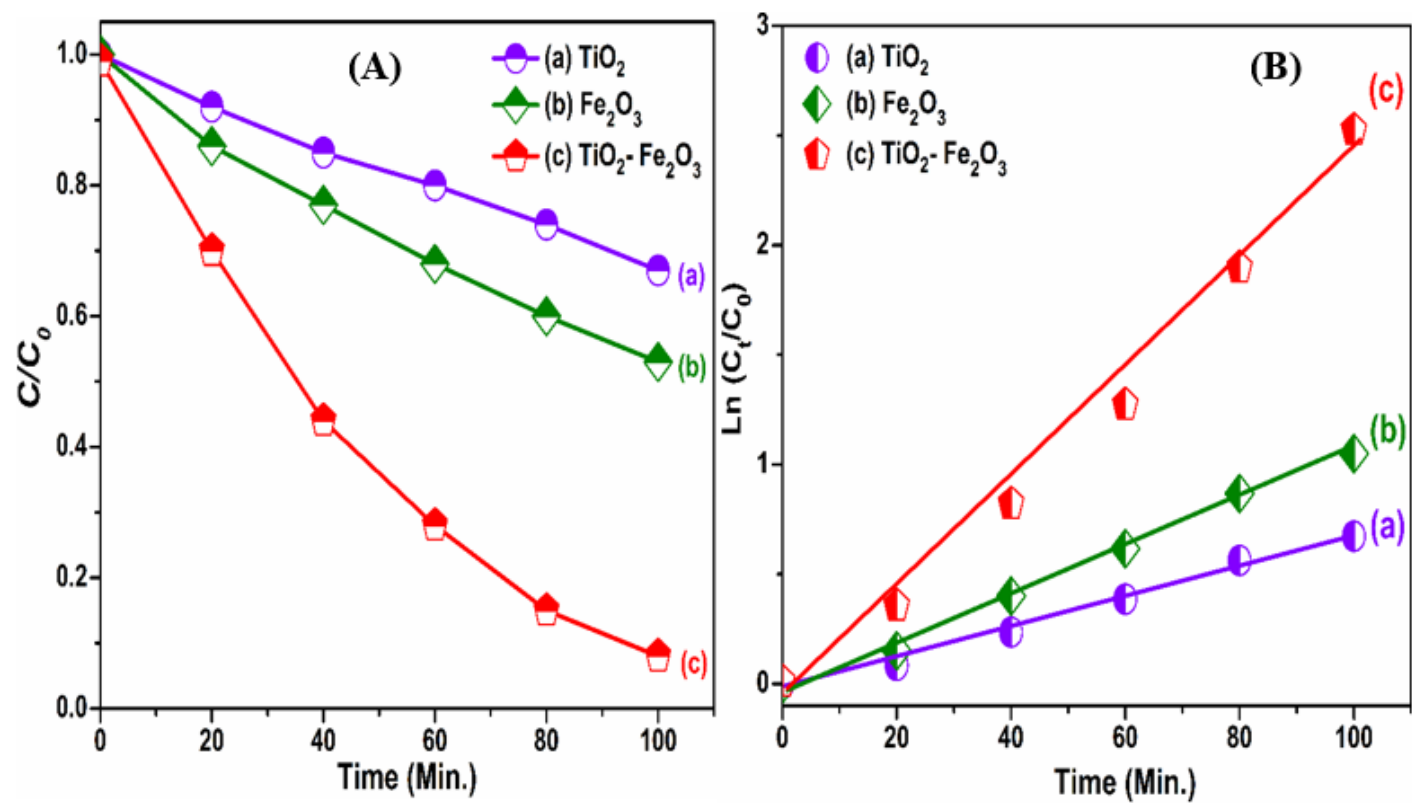


Figure 8

(A) Photodegradation efficiency of MB dye (B) First-order kinetic fitting plots $-\ln (C_0/C_t)$ versus reaction time t for the as-obtained different PCs

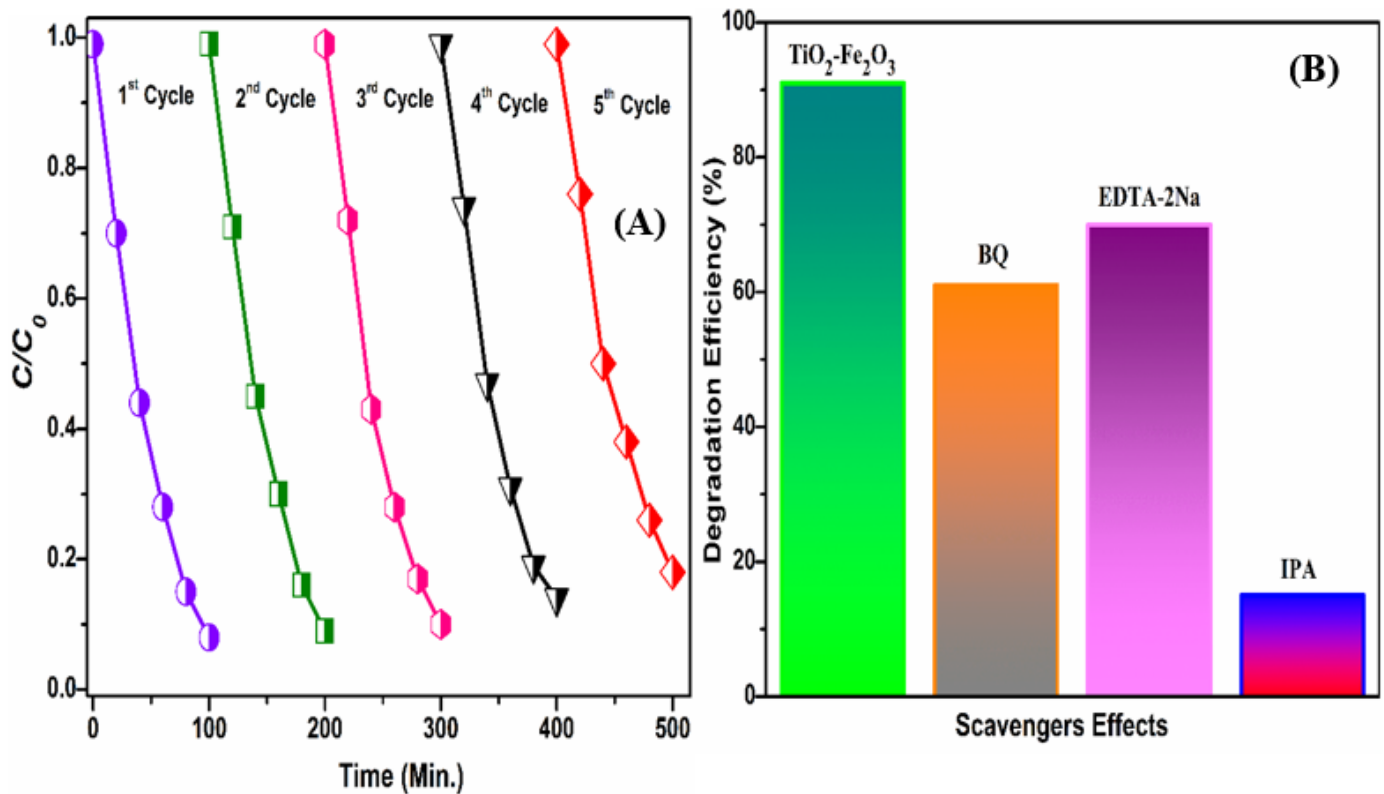


Figure 9

(A) Photocatalytic recycling stability of energetic TiO₂/α-Fe₂O₃ PCs and (B) Photodegradation of MB aqueous dye over as-obtained TiO₂/α-Fe₂O₃ composite catalyst in the existence of dissimilar scavengers

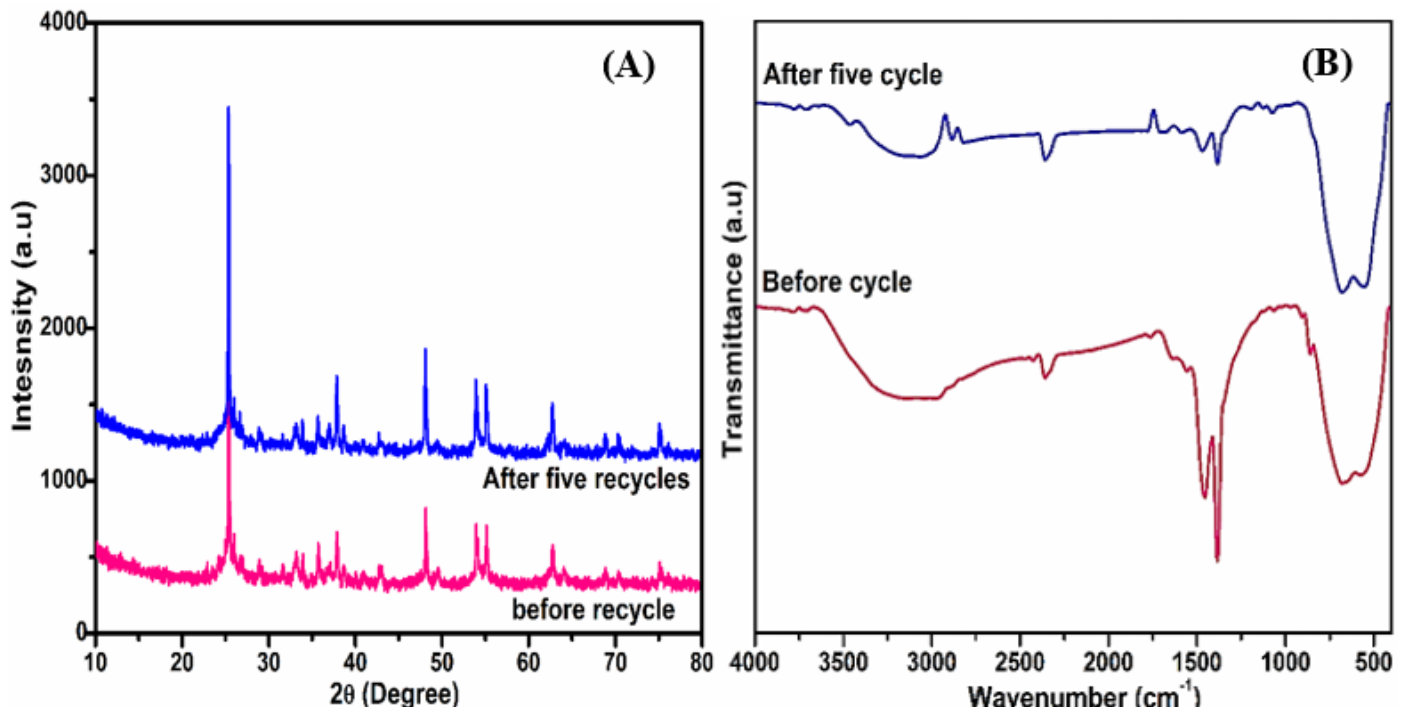


Figure 10

(A) XRD pattern and (B) FT-IR spectra of TiO₂/α-Fe₂O₃ composite catalyst by before (a) and after (b) recycling process

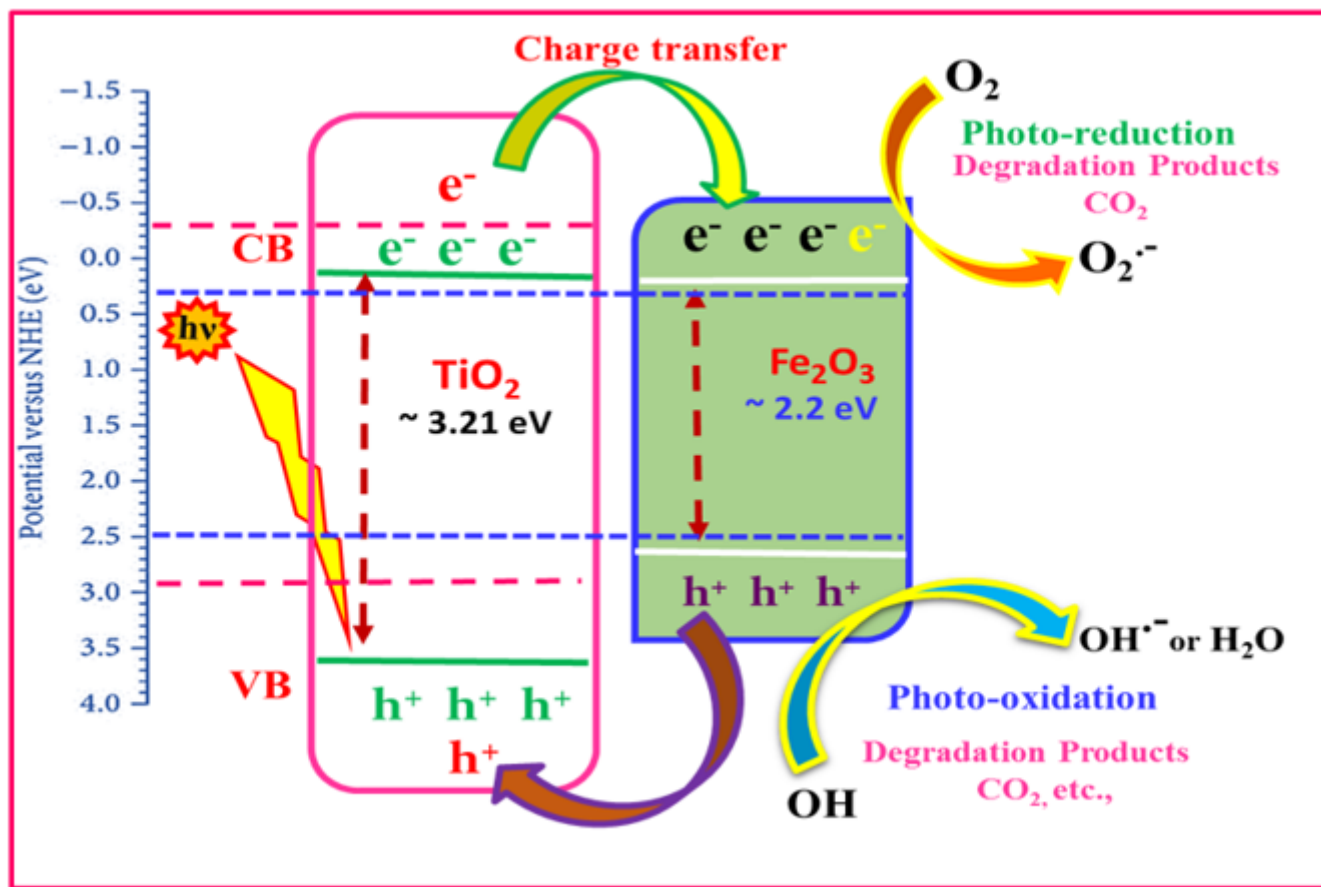


Figure 11

Photocatalytic mechanisms for schematic diagram of TiO₂/α-Fe₂O₃ heterostructure composite catalyst under visible-light exposure